Available online at www.sciencedirect.com

SCIENCE DIRECT®

Nuclear Instruments and Methods in Physics Research A 499 (2003) 75–99

NUCLEAR INSTRUMENTS & METHODS IN PHYSICS RESEARCH Section A

www.elsevier.com/locate/nima

The interaction region of KEKB

K. Kanazawa, H. Nakayama, T. Ogitsu, N. Ohuchi, T. Ozaki,
K. Satoh, R. Sugahara, M. Tawada, N. Toge, K. Tsuchiya*,
Y. Yamada, M. Yoshida, M. Yoshioka

High Energy Accelerator Research Organization (KEK), Oho 1-1, Tsukuba, Ibaraki 305-0801, Japan

---

Abstract

An asymmetric-energy collider of 8 GeV electrons and 3.5 GeV positrons, KEKB, has been operating at KEK since 1998. On July 9, 2001 it achieved the highest record of luminosity, 4.5×10^{33} cm^{-2} s^{-1}. This paper describes the interaction region (IR) extending about 8 m from the interaction point (IP) along each beam direction. The main machine components in the IR are focusing quadrupole magnets, compensation solenoids, and vacuum chambers, which are positioned on movable stages. They are designed to focus both beams into collisions with a finite angle crossing.

PACS: 29.20

Keywords: Collider; Storage ring; Interaction region; Superconducting magnet; Special quadrupole magnet; Be vacuum chamber

---

1. Introduction

The KEK B-Factory, KEKB, is an asymmetric-energy, two-ring, electron–positron collider for *B* physics [1,2]. The 8 GeV electrons stored in a high-energy ring (HER) and the 3.5 GeV positrons in a low-energy ring (LER) collide at one interaction point (IP) with a finite angle of ±11 mrad; the Belle detector, having a 1.5 T solenoid [3], surrounds it. The features of this interaction region are a finite angle crossing of the beams and a superconducting final focusing magnet system, which includes a compensation solenoid. The large crossing angle helps to separate the two beams quickly, which allows a small bunch spacing, and hence the smallest parasitic crossing. The large angle crossing also helps to minimize the bending of the incoming beams, which minimizes the synchrotron radiation that can enter the detector and cause detector backgrounds. The superconducting final focusing system introduces flexibility of machine tuning. A compensation solenoid, which is positioned in front of the final focusing quadrupole, helps to reduce any x–y coupling effects due to the detector solenoid, and consequently to improve the dynamic aperture and the luminosity.

The designed beam parameters related to the IP [1] and their achieved values by the middle of July 2001 are listed in Table 1.

A schematic layout of the beam line near the IP is shown in Fig. 1. This figure shows four superconducting magnets (S-R, S-L, QCS-R and

---

*Corresponding author.

E-mail address: kiyosumi.tsuchiya@kek.jp (K. Tsuchiya).

0168-9002/03/$ - see front matter
PII: S0168-9002(02)01784-9

Table 1
Design beam parameters related to the interaction point

	LER		HER
Energy (GeV)	3.5		8.0
Current (mA)	2600 (845)		1100 (715)
Crossing angle (mrad)		11×2	
Luminosity (cm^{-2} s^{-1})		1×10^{34} (4.49×10^{33})	
Bunch spacing (m)		0.59 (2.4)	
β_x^* (m)	0.33 (0.59)		0.33 (0.63)
β_y^* (m)	0.01 (0.0065)		0.01 (0.0065)

The figures in parentheses are the values when the highest luminosity was achieved in July 2001.

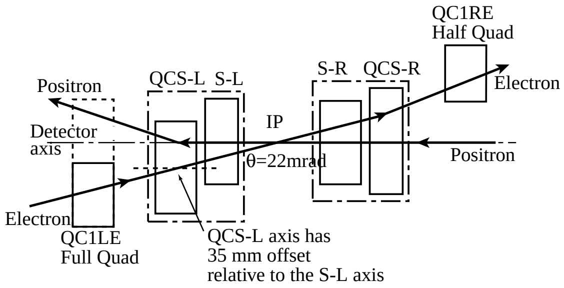

Fig. 1. Layout of the beam line near the IP.

QCS-L) and two normal-conducting quadrupole magnets (QC1RE and QC1LE). The final vertical focusing of the two beams is provided by a pair of superconducting quadrupoles (QCS-R and QCS-L). The solenoids (S-R and S-L) are for compensating a solenoid field created by the Belle detector. The QCS and S magnets on each side of the IP are contained in a common cryostat. The vertical focusing strength of QCS is tuned to the 3.5 GeV positron beam. Extra vertical focusing for the 8 GeV electron beam is provided by a pair of special quadrupole magnets (QC1RE and QC1LE). The geometries of these quadrupoles were designed such that only the electron beam would see the quadrupole fields when passing through them. Positrons enter the IP through QCS-R and leave through QCS-L. Electrons proceed in the opposite direction. Since the two beams pass through the same bores of the QCS magnets and collide at the IP with a finite crossing angle of 2 × 11 mrad, one beam must go off-axis in the QCS magnets. To minimize the synchrotron radiation background near the IP, the incoming positron beam axis was set on the magnetic axes of S-R and QCS-R. Likewise, the incoming electron beam axis was set on the QCS-L axis, which was shifted by 35 mm with respect to the axis of S-L. The axes of S-L and S-R were aligned to the detector solenoid axis in order to maintain the axial symmetry of the field in the Belle detector.

Fig. 2 shows a top view of the main accelerator element layout in the IR. As can be seen in this figure, the locations of the cryostats containing the QCS and S magnets are completely inside the detector. Therefore, they must be compact and rigidly supported to withstand the large electromagnetic forces applied to the coils from the 1.5 T detector solenoid. A service duct, which comes out from the cryostat, is connected to a service cryostat, which is located outside the detector. The QC1RE and QC1LE magnets are located near the outer edges of the detector structure. Due to the limited beam separation at the right side of the detector, QC1RE was designed as a half-quadrupole magnet. The QC2RE and QC2LE magnets provide the horizontal focusing of the electron beam and QC2RP and QC2LP provide that of the positron beam. Like the QC1LE magnet, these magnets are also iron-dominated normal conducting magnets, and have a field-free channel for the beam of the other ring. The QCS magnet cryostat is supported from a movable stage. This movable stage serves as a common support base for the special quadrupole magnets. The stage can move along the beam line by approximately 4 m, so that the QCS magnets can be pulled out for maintenance of the detector elements.

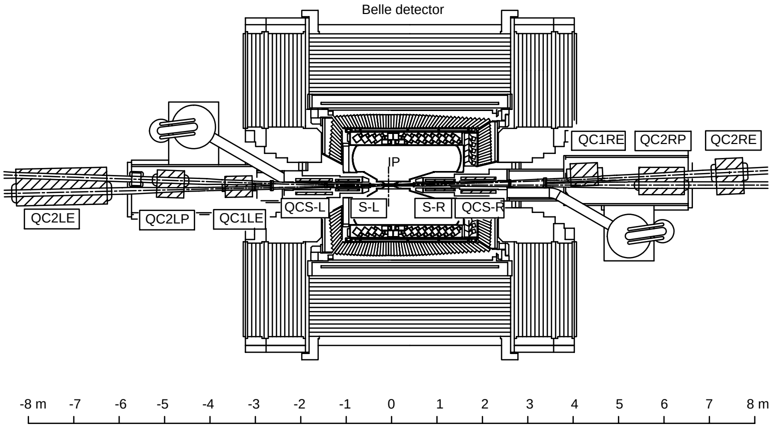

Fig. 2. Layout of the beam line near the IP.

2. Precision IR movable tables

There are two precision IR movable tables at the IR, one on the left side of the IP and the other on the right side. The QCS magnet and three normal conducting quadrupole magnets (special quadrupole magnets) are fixed on each table. These tables can move back and forth along the center axis of the Belle detector with high precision. By this movement, the QCS magnets can be inserted into or extracted from the Belle detector. The IR movable table consists of four square-shaped pipes sandwiched between 30 mm-thick top and bottom plates. The cross-section and the thickness of these square-shaped pipes are $350 \times 350\ \mathrm{mm}^2$ and 12 mm, respectively. Two pipes are on one side and the other two are on the other side. The pipes on each side are connected to each other by short square-shaped pipes at five points. Their material is non-magnetic 304 stainless steel. They are welded to each other. The table is driven by a rack-and-pinion mechanism. A rack gear is installed on one side of the table and the pinion gear is fixed on the floor. The pinion gear is driven by an inverter-controlled synchronous motor. The movement is guided by LM guides (consisting of precision rails and linear motion bearings). The speed is switched from high to low speed, or vice-versa, by limit switches installed near both ends of the guide rails, and stop boards are installed as well at both ends. Start/stop and speed are controlled by pushing buttons on the control pendant. The specifications and performance of these precision tables are listed in Tables 2 and 3, respectively.

Table 2
Specifications of precision IR movable tables

Item	L side	R side
Total length (mm)	5150	5600
Width (mm)	1200	1200
Height (mm)	1110	1110
Range of movement (mm)	3450	4240
Speed high (m/s)	2	2
low (m/s)	0.3	0.3
Weight (t)	8.9	9.6

Table 3
Performance of precision IR movable tables

Item	Specification	L side	LR side
Reproducibility of stop position			
Longitudinal position (mm)	0.1	0.01	0.01
Transverse position (mm)	0.1	0.02	0.02
Transverse errors in movement			
Vertical error (mm)	2.0	0.2	0.1
Horizontal error (mm)	2.0	0.2	0.3
Natural frequency (Hz)>	10	17	20

3. Superconducting magnet system

The superconducting magnet system consists of two compensation solenoids (S-R and S-L), two final focusing quadrupoles (QCS-R and QCS-L), and six correctors [4–6]. These magnets are installed completely inside the detector solenoid and are operated under a detector solenoid field of 1.5 T [3]. The QCS magnet, solenoid, and three types of correctors on each side of the IP are contained in a compact common cryostat. Cross-sectional views of the magnet cryostat are shown in Figs. 3 and 4. QCS-R and QCS-L are tuned to the positron beam energy, 3.5 GeV, and are located at 1920 and 1600 mm (magnet center position) from the IP, respectively. The quadrupole center of QCS-R is on the incoming beam (positron beam) axis, while that of QCS-L is shifted by 35.1 mm horizontally from the positron beam axis. In addition, the QCS-R and QCS-L have roll angles of −33.2 and 10.4 mrad, respectively, in order to cancel the skew components

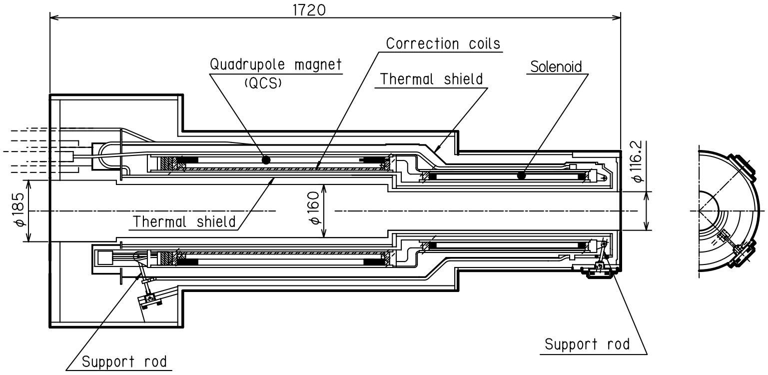

Fig. 3. Longitudinal cross-section of the QCS-L magnet cryostat.

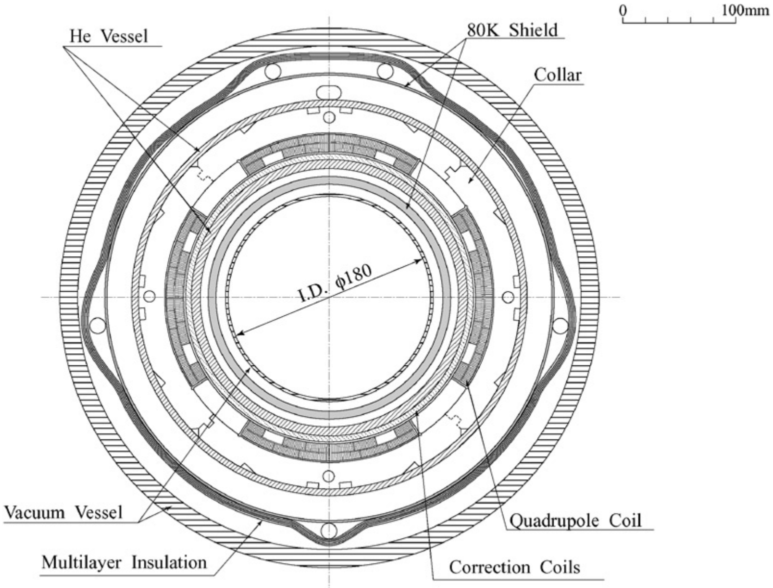

Fig. 4. Cross-sectional view of the QCS magnet cryostat.

from the detector solenoid field at their locations. QCS-R and QCS-L are connected in series via superconducting bus lines. They are excited with a main power supply and an auxiliary power supply, which can feed a current only to QCS-R. S-R and S-L are designed to cancel the integral field of the axial component, B_z, by the detector solenoid. They are placed in the front of the QCS magnets. Three kinds of correction coils are installed inside the magnet bore of the QCS, as shown in Fig. 4. These coils can be used to shift the quadrupole center and to rotate the quadrupole field. These magnets on both sides are cooled in parallel by sub-cooled liquid helium at 4.5 K and 0.15 MPa.

Table 4
Main design parameters of QCS-R and QCS-L

	QCS-R	QCS-L
Field gradient, G (T/m)	21.73 (21.84)	21.66 (21.84)
Effective magnetic length (mm)	385 (387.7)	483 (486.1)
Magnet operating current (A)	2963	2963
Maximum field on the conductor (T)	4.3	4.3
Coil length, (mm)	521	617
Coil inner radius (mm)	130	130
Coil outer radius (mm)	144.9	144.9
Stored energy (kJ)	63.7	80.0

The figures in parentheses are measured values.

3.1. Final focusing quadrupole magnet (QCS-R and QCS-L)

QCS-R and QCS-L are iron-free magnets. Their design is based on a set of $\cos 2\theta$ windings, which consists of two-layer coils, as shown in Fig. 4. The main parameters of QCS-R and QCS-L are listed in Table 4. The coils have large apertures of 260 mm, and are clamped with stainless-steel collars. The coil lengths of QCS-R and QCS-L are 521 and 617 mm, respectively. A quadrant coil and the collar of the QCS-R magnet are shown in Fig. 5. These quadrupoles are rather short and have large apertures. Therefore, more than half of the coil length is occupied by the coil ends. Table 5 lists, the main parameters of the NbTi/Cu superconducting cable. It is a keystoned Rutherford cable, which consists of 24 multi-filamentary strands. The cable is insulated with two types of Upilex tape, 25 and 50 μm in thickness. Since the critical current density of this conductor is rather high ($J_{c_{\mathrm{NbTi}}} = 2800\ \mathrm{A/mm^2}$ at 5 T, 4.2K), the design current of these QCS magnets corresponds to 71% of the cable critical current under an external field of 1.5 T.

The required field gradient of QCS-R and QCS-L was 21.84 T/m, and their integral higher multipole fields should be less than 1×10^{-4} of the quadrupole field at a radius of 40 mm. By a two-dimensional calculation, a good solution, whose b_6

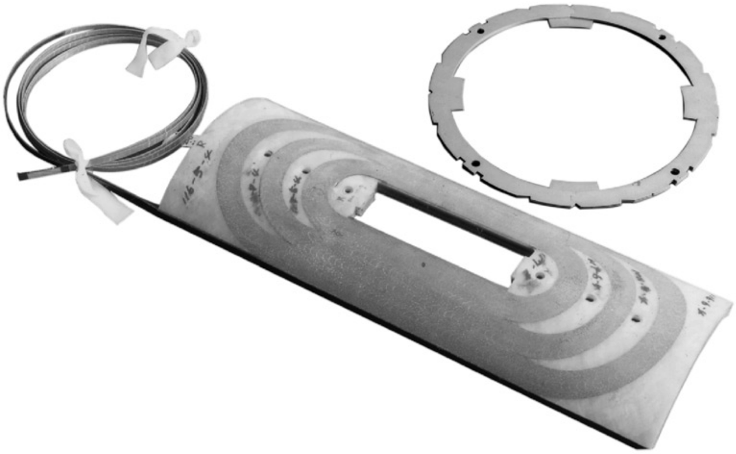

Fig. 5. A quadrant coil and collar for the QCS-R magnet.

Table 5
Parameters of superconducting cable

Strand diameter (mm)	0.589
Filament diameter (μm)	6.4
Surface condition	Coated with Sn-5Ag
RRR of stabilizing copper	155–169
Copper ratio, Cu/Sc	1.75 – 1.82
Cable height (mm)	7.006 ± 0.009
Mid thickness (mm)	1.089 ± 0.003
Number of strands	24
Cable twist pitch (mm)	61.5
Critical current at 5 T and 4.2 K (A)	6620
at 6 T and 4.2 K (A)	5210

Table 6
Integral multipole (nth) coefficients of QCS-R and QCS-L at $R = 40$ mm and magnet center

QCS-R			QCS-L	
n	a_n	b_n	a_n	b_n
1	−0.37	0.00	−0.23	0.00
2	−0.00	10000.	0.00	10000.
4	−0.00	0.23	−0.00	0.18
6	−0.00	−0.01	0.00	0.03
10	−0.00	−0.03	0.00	−0.02

Table 7
Effects of fabrication errors at $R = 40$ mm

Parameters changed	$\Delta G/G$ 10^{-4}	Δb_6 10^{-4}	Δb_{10} 10^{-4}
Radius of inner coil	−33.0	−0.09	−0.00
Radius of outer coil	−39.0	0.09	0.00
Radius of inner No. 1 coil	−27.0	−0.35	0.00
Radius of inner No. 2 coil	−6.0	0.27	−0.00
Pole angle of inner coil	5.0	−0.01	−0.00
Pole angle of outer coil	17.0	0.25	−0.00
Wedge of inner coil	−11.0	−0.33	−0.00

and b_{10} are -4.2×10^{-6} and 3.1×10^{-7}, respectively, was found; coil-end optimization was then performed. As mentioned above, the magnet has a large aperture of 260 mm and a short length. The length of the straight section is 201 and 300 mm for QCS-R and QCS-L, respectively. Therefore, the integral field quality of the magnet is strongly influenced by the error fields in the coil ends. The configuration of the coil ends was designed so that the integral multipole coefficients would be less than 1×10^{-4} at a radius of 40 mm. During the optimization process, the effect of the splices and the transition of the cables from the first layer to the second layer was taken into account. Especially, in order to exclude a skew quadrupole component in the lead end, two quadrant coils were wound clockwise and two other coils were wound anticlockwise; they were then assembled alternately. Introducing this winding scheme, the peak value of a_2 in the magnet lead end was reduced from 1.9×10^{-3} to 3×10^{-6} at a radius of 40 mm. The integral multipoles of the QCS magnets are shown in Table 6.

The skew dipole components come from the splice in the magnet end and b_4 comes from the lead end. The other integral multipole coefficients not shown in the table are less than 1×10^{-6}.

The effects of any coil fabrication errors on the multipole components were studied by two-dimensional calculations, assuming a basic eight-fold symmetry in the coil geometry and errors of 0.5 mm in each direction [4]. The results are summarized in Table 7. As can be seen from this table, the changes of b_6 and b_{10} due to the assumed errors are very small (less than 1×10^{-4}); however, the change of the field gradient, $\Delta G/G$, due to a 0.5 mm change of the coil radius is about 4×10^{-3}.

Various forces exerted on each coil when they are excited in various external fields were studied by Biot-Savarts law. Table 8 gives the major forces and torques that act on each coil.

3.2. Compensation solenoids (S-R and S-L)

The main parameters of S-R and S-L are summarized in Table 9. The lengths of S-R and S-L are 616 and 461 mm, respectively, but they have the same inner radius of 95 mm. The designed field strengths at the centers of S-R and S-L were 616 and 461 T, respectively. Monolithic NbTi/Cu superconducting wire was used for the coil. The wire cross-section was 1.1 mm × 1.9 mm, and the Cu/Sc ratio was 1.0. For electrical insulation, a resin in a polyimid group was used because of its strength against radiation damage. The thickness of the insulation was 40 μm. The

Table 8
Major electromagnetic forces and torques work on each coil

	F_x	F_y	M_x	M_y	M_z
QCS-L	−1 kN (Yoke)	0.8 kN (Det.) 1 kN (S-L)	0.2 kNm (Det.) −0.5 kN m (S-L)		
ND-L	51.8 kN (Q-L)	−1.8 kN (Det.) 0.2 kN (S-L)	1.1 kN m (Det.) −0.1 kN m (S-L)		
SD-L	−1.9 kN (Det.) 0.2 kN (S-L)	55.2 kN (Q-L)		−1.2 kN m (Det.) 0.1 kN m (S-L)	
SQ-L					4.8 kN m (Q-L)
ND-R	42.4 kN (Q-R)	0.4 kN (Det.) −0.2 kN (S-R)	2.3 kN m (Det.) −0.1 kN m (S-R)		
SD-R	0.4 kN (Det.) −0.2 kN (S-R)	45.3 kN (Q-R)	−2.4 kN m (Det.) 0.1 kN m (S-R)		
SQ-R					3.8 kN m (Q-R)

ND, SD, and SQ are the normal dipole, skew dipole, and skew quadrupole correctors, respectively. The coil and the detector yoke, which produce the force and/or torque, are shown in parentheses. Det., S-R, S-L, and Q correspond to the detector solenoid, the right side and left side compensation solenoids, and the QCS magnets.

Table 9
Main parameters of S-R and S-L

	S-R	S-L
Central field (T)	5.80	4.53
Operating current, Iop (A)	603	487
Maximum field on the conductor (T)	5.83	4.59
$I_{\mathrm{op}}/I_{\mathrm{c}}$ at 4.5 K (%)	75	58
Coil length (mm)	616	461
Coil inner radius (mm)	95	95
Coil outer radius (mm)	115	115
No. of turns	4912	3696
Stored energy (kJ)	258	115

coils were impregnated with epoxy resin under pressure after being wound on the inner cylinder, and enclosed in helium vessels while applying axial compression forces of 516 and 250 MN to S-R and S-L, respectively. The designed operating currents were 603 and 487A for S-R and S-L, respectively, and their ratios to the critical current of short sample wires were 75% and 59%.

Since S-R and S-L are operated in the opposite field of the Belle solenoid, the maximum field on the conductor is reduced by 1.5 T from the values listed in Table 9, and axial repulsive forces work on these solenoids. The calculated forces on S-R and S-L are 2.8 and 22 kN, respectively. When these magnets are excited, the electromagnetic force acting on the solenoids changes from a compression force to a bursting force [5]. In order to manage these forces, the coils were wound under a tension of 18 kgf and a rather thick bobbin (helium inner cylinder) of 7 mm was selected.

3.3. Correction coils

Three types of correction coils, namely, a skew quadrupole coil and normal and skew dipole coils, are embedded inside the bore of the QCS magnets. The parameters of these coils are listed in Table 10. The field strengths of the dipoles and the skew quadrupole at 50 A are 0.05 T and 0.44 T/m, respectively. The correction coils for QCS-R and QCS-L have the same geometry, while the magnetic lengths of QCS-R and QCS-L are different. Therefore, the capacity to rotate the

Table 10
Design parameters of correction coils

	Skew quad.	Normal dipole	Skew dipole
Transfer function at 40 mm and 50 A (Tm)	0.00871	0.0244	0.0242
Alignment capacity of mag. center shift (mm)		±3.0/±2.4	±3.0/±2.4
Alignment capacity of mid-plane angle (mrad)	±12.7/±10.2		
Design current (A)	50	50	50
No. of turns/pole	100	212	212
Coil length (mm)	560.6	565	560.5
Coil inner radius (mm)	123.5	126.9	125.2
Stored energy (J)	28.7	63.0	54.7

Alignment capacity for correction in a column is for QCS-R and QCS-L, respectively.

quadrupole field and to shift its center are different, as shown in Table 10. The coils at the maximum operating current, 50 A, have a rather large margin ($I/I_c < 50\%$), although they are operated in a combined field of the quadrupole field (3.2 T) and solenoid field (1.5 T).

Each correction coil is one layer and a flat coil with a substrate. The flat coils were fabricated at BNL using a multi-wiring technique [7]. The coils were set on the 8 mm-thick stainless-steel cylinder of the helium vessel by a Japanese company. The total thickness of the three correction coils, including the insulation and the bindings, was 6.6 mm. Since these coils were used to align the magnetic center and the mid-plane of QCS-R and QCS-L to the beam lines, the axial centers and mid-planes of the coils were aligned to those of QCS-R and QCS-L. The precision of the coil alignment was expected to be within ±1 mm.

A multi-filament NbTi/Cu superconducting wire of 0.33 mm diameter was used for the coils. The ratio of copper to NbTi in the wire was 2.5. The wire was insulated with 25 μm-thick Kapton.

As shown in Table 8, the correction coils have a large interaction with QCS-R and QCS-L. An 8 mm-thick support cylinder was selected to withstand the electromagnetic force. The interaction between the dipole coils and the QCS field causes a horizontal or vertical deformation of the support cylinder. This deformation was calculated to be 74 μm, and its effect on the dipole corrector field was estimated to be negligible. In the case of the skew quadrupole coil and the QCS field, a torque works on the coil. However, the twist of the coil is less than 10 μrad due to the thick support cylinder.

3.4. Magnetic field of the superconducting magnets

Field measurements were performed after installing the magnets in the IR [8,9]. The magnetic fields of QCS-R, QCS-L, and the correction coils were measured by using two harmonic coils. The lengths of the harmonic coils were 800 and 50 mm. The 800 mm-long harmonic coil was used to measure the integral fields of the magnets, while the 50 mm-long harmonic coil was used to measure the field profiles along the magnet axis. The solenoid field was measured by a Hall probe calibrated by an NMR probe. These measurements were performed along the positron beam axis.

The measured field gradient of both QCS-R and QCS-L was 21.84 T/m, and the effective magnetic lengths were 387.7 and 486.1 mm, respectively. The measured field gradients were slightly higher than the calculated values. These differences were considered to be mainly attributable to a change in the coil radius due to thermal shrinkage. The rotations of the quadrupole field of the QCS-R and QCS-L magnets were −35.55 and 10.82 mrad, while the design values were −33.16 and 10.48 mrad, respectively. These alignment errors are within the capacity of the skew quadrupole correctors, as shown in Table 10. The integral field characteristics of QCS-R and QCS-L are shown in Figs. 6 and 7, respectively. The major multipole

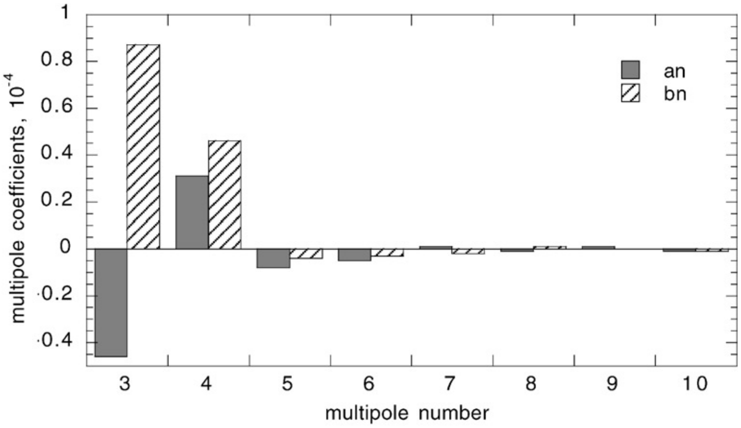

Fig. 6. Integral multipole coefficients of QCS-R at 3000 A and $R = 40$ mm.

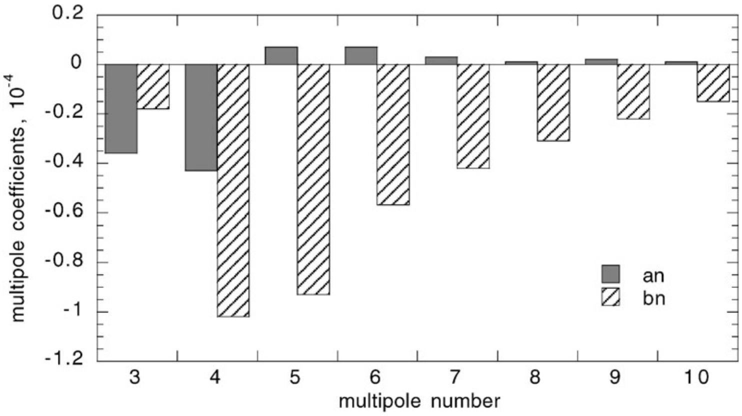

Fig. 7. Integral multipole coefficients of QCS-L at 3000 A and $R = 40$ mm.

components of QCS-R were the sextupole and octupole fields. Since the magnetic field of QCS-L was measured with a horizontal off-set of 35.1 mm, the multiple coefficients of QCS-L were different from those of QCS-R. However, the multipole coefficients of both magnets were less than 1×10^{-4}.

Since the beta functions of the beams change rapidly in the QCS magnet, precise field profiles along the beam lines were required. These profiles were measured with the 50 mm-long harmonic coil by moving the coil every 1 cm along the positron beam axis. Typical results at a radius of 40 mm are shown in Fig. 8. The axis of the abscissa shows the distance from the IP, and the plus and minus signs of the values correspond to the right and left side of the IP, respectively. Since QCS-L was measured at the position of 35.1 mm shifted from the magnetic center, a large dipole coefficient, b_1, appeared, and also the local peaks of b_6 reached -10×10^{-4} in the coil ends, although the integral value along the whole magnet was less than 1×10^{-5}. In b_{10}, the same peaks could be seen in the coil ends, and the value was 0.26×10^{-4}. The behavior of the multipole components along the beam line was quite consistent with the calculation.

Fig. 9 shows the B_z profile along the positron beam axis when S-R, S-L, and the Belle solenoid were excited together. The open circles show the

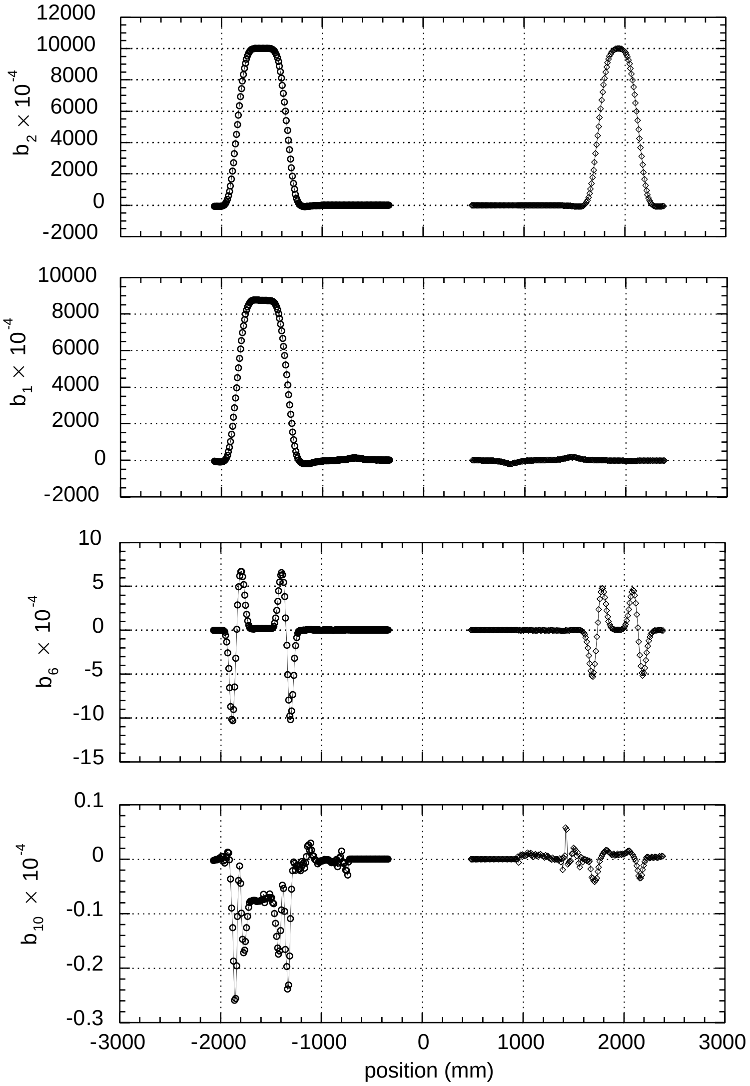

Fig. 8. Profiles of b_2, b_1, b_6, and b_{10} multipole coefficients of QCS-L and QCS-R along the beam line. The origin of the horizontal axis corresponds to the interaction point.

measured values. Since it was not possible to complete the measurement along the whole beam line because of the spatial constraint, a model that reproduced the same field profile as the measurement was constructed and the operating currents of S-R and S-L were determined by using this model.

The fields of the correction coils were measured with the harmonic coils. The measured results for GL and BL are given in Table 11. The coils can generate sufficient magnetic fields to correct the misalignments of QCS-R and QCS-L. The alignment errors of the coils to the QCS fields were measured with the harmonic coils. The skew quadrupole and the normal dipole on the right side had large errors of -27.43 and -13.04 mrad, respectively. In order to cancel these errors and obtain pure quadrupole and dipole fields by the correctors, the coil currents (I) were chosen using the 8×8 matrix expressed in the following

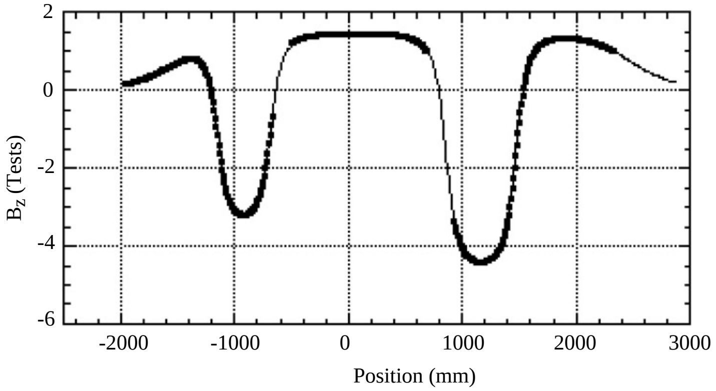

Fig. 9. B_z distribution along the beam line. The solid lines show the calculated distribution. Open circles correspond to the measured results when SR, SL, and the Belle solenoid were excited together.

equation:

$$\begin{bmatrix} I_{\text{ND-L}} \\ I_{\text{SD-L}} \\ I_{\text{SQ-L}} \\ I_{\text{QC-S}} \\ I_{\text{ND-R}} \\ I_{\text{SD-R}} \\ I_{\text{SQ-R}} \\ I_{\text{QCS-AUX}} \end{bmatrix} = \begin{bmatrix} a & b & c & d & 0. & 0. & 0. & 0. \\ e & f & g & h & 0. & 0. & 0. & 0. \\ i & j & k & l & 0. & 0. & 0. & 0. \\ m & n & o & p & 0. & 0. & 0. & 0. \\ 0. & 0. & 0. & 0. & q & r & s & t \\ 0. & 0. & 0. & 0. & u & v & w & x \\ 0. & 0. & 0. & 0. & y & z & aa & ab \\ -m & -n & -o & -p & ac & ad & ae & af \end{bmatrix} \times \begin{bmatrix} SK0_{\text{L}} \\ K0_{\text{L}} \\ SK1_{\text{L}} \\ SK0_{\text{R}} \\ K0_{\text{R}} \\ SK1_{\text{R}} \\ SK1_{\text{R}} \\ K1_{\text{R}} \end{bmatrix}, \tag{1}$$

Table 11
Measured results for the correctors

	Design	Left	Right
Skew quadrupole GL (T/m m)	0.2174	0.2120	0.2122
Alignment error (mrad)	0.	0.22	−27.43
Skew dipole BL (T m)	0.0244	0.0255	0.0250
Alignment error (mrad)	0.	4.59	3.85
Normal dipole BL (T m)	0.0242	0.0253	0.0247
Alignment error (mrad)	0.	1.57	−13.04

where the subscripts of ND, SD, and SQ correspond to the normal dipole, skew dipole, and the skew quadrupole. L and R signify the coils on the left and right sides, respectively. $I_{\text{QCS-AUX}}$ is the current of the auxiliary power supply in order to tune the integral field gradient of the QCS-R magnet. In this matrix, the values shown with letters were chosen from the field measurement data.

3.5. Cryostat

Severe spatial constraints were imposed on the cryostat design, and very compact cryostats had to be built, because they are placed almost completely inside the detector. In addition, in the case of the left-side cryostat, the quadrupole axis had to be shifted horizontally by 35 mm from the solenoid axis. This introduced significant difficulty in the fabrication and assembly. Fig. 10 shows a schematic view of the left-side cryostat [10]. The cryostat system consists of three parts: a horizontal annular vessel (magnet cryostat) containing the magnets, a service cryostat, and a service duct connecting both cryostats. The helium vessel is made of 316L stainless steel. The inner cylinder works not only as a part of the pressure vessel, but also as a mechanical support for the coils. The helium vessel is surrounded by a thermal-radiation shield. The outer shield consists of a stainless-steel shell with a cooling pipe, while the inner shield consists of a 7 mm-thick 316L stainless-steel cylinder with helical grooves for liquid nitrogen. About 30 layers of aluminized Kapton were arranged between the vacuum vessel and the thermal shield. However, since the spatial separation between the helium vessel and the thermal shield is limited (6–7 mm gap), no superinsulation was installed. The outer cylinder of the vacuum vessel functions as the mechanical frame of the suspension system for the helium vessel, and the thickness of the cylinder is 16 mm.

The helium vessel containing the magnets is suspended by eight support rods in the vacuum vessel. The rods are made of titanium alloy, Ti–6Al–4V [ELI], which has a high ultimate tensile strength and a low thermal conductivity. Since various electromagnetic forces act on the magnets due to interaction with the detector solenoid field, the support rods must withstand these forces. In the case of the left-side cryostat, the stress in the rods was estimated to be 294 N/mm^2 due to the large axial force acting on S-L.

The service cryostat functions as an interface between the cryostat and the multi-channel transfer line coming from the sub-cooler. The top of the service cryostat is equipped with bayonet joints for the transfer lines, two control valves, current leads for the S solenoids and correction coils, and some service ports. The current leads for the QCS magnets are on the sub-cooler box. In the service cryostat, the superconducting bus lines from both the sub-cooler and the QCS magnet are connected by soldering.

The calculated thermal loads on the liquid helium are given in Table 12. The total loads of the right- and left-side cryostats are 14.23 and 13.78 W, respectively. These loads are small enough to keep the liquid helium in the cryostat in a sub-cooled state. During a performance test, the heat load of each cryostat was evaluated by measuring the enthalpy increase of the sub-cooled liquid helium. The values were 12.4 and 9.0 W for the right- and left-side cryostats, respectively. These are slightly less than the design values.

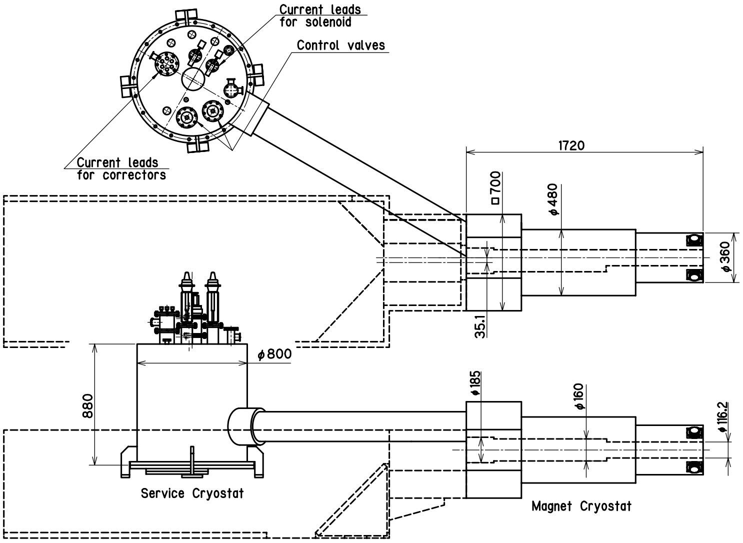

Fig. 10. Magnet cryostat and service cryostat for the QCS-L magnet.

Table 12
Calculated thermal loads of the cryostats

		Right side (W)	Left side (W)
Magnet cryostat	Radiation	0.94	0.87
	Conduction thr. support rods	3.38	3.18
Transfer tube between cryostats	Radiation	0.56	0.38
	Conduction thr. FRP supports	0.77	0.77
Service cryostat	Radiation	0.33	0.33
	Conduction thr. bayonet joints	2.12	2.12
	Conduction thr. tubing	2.81	2.81
	Conduction thr. valves	0.54	0.54
	Conduction thr. signal wires	2.78	2.78
Total		14.23	13.78

3.6. Cooling system

The main components of the cooling system are those of the TRISTAN mini-beta insertion quadrupole magnets [11], although the cryostats and some parts of the transfer lines were renewed. The refrigerator has a cooling capacity of 153 W + 30 L/h at a temperature of 4.4 K. The cooling system can produce sub-cooled liquid helium of 25 g/s as a coolant for the magnets. The individual thermal loads of the system components are given in Table 13. The calculated total load was 75 W + 29 L/h. The margin of the cooling capacity for operation was estimated to be 80 W.

The sub-cooled liquid helium is transferred from the sub-cooler to two magnet cryostats via parallel cryogenic multi-channel transfer lines. The total length of the transfer line is 37 m. A cross-section of the transfer line is shown in Fig. 11. It contains five lines (LHe flow and return lines, He bypass line, LN_2 flow and return lines). Fully stabilized superconducting bus lines with a capacity of 3500 A are installed in the LHe flow line.

Fig. 12 shows the temperature changes of the QCS magnets during the cool-down process. The magnets on both sides were cooled down from room temperature with parallel cooling circuits. The helium gas temperature was controlled in order to decrease the magnet temperature gradually. To operate the magnets, the liquid-helium level in the sub-cooler must be higher than 55% in order to keep the temperature of the sub-cooled liquid helium below 4.5 K. The cool-down process takes about 27 h. Fig. 13 shows the recovery of the system after magnet quenching. It takes about 50 min to cool the magnets and 4 h to recover the liquid-helium level.

Table 13
Thermal loads of the cooling system

Thermal load (design)	Current lead (QCS magnet: 3500 A) × 2	14 L/h
	Current lead (QCS magnet: 100 A) × 1	1 L/h
	Current lead (S magnets: 650 A) × 4	7 L/h
	Current lead (corrector: 100 A) × 12	7 L/h
	Cryostat × 2	35 W
	Multi-cryogenic transfer tube (25 m)	20 W
	U-type cryogenic transfer tube (6.3 m × 2)	20 W
Total		75 W +29 L/h

3.7. Electrical system

A schematic diagram of the electrical circuit is shown in Fig. 14. The SCR power supply for the QCS magnets is composed of a main power unit (3500 A, 15 V) and an auxiliary power unit

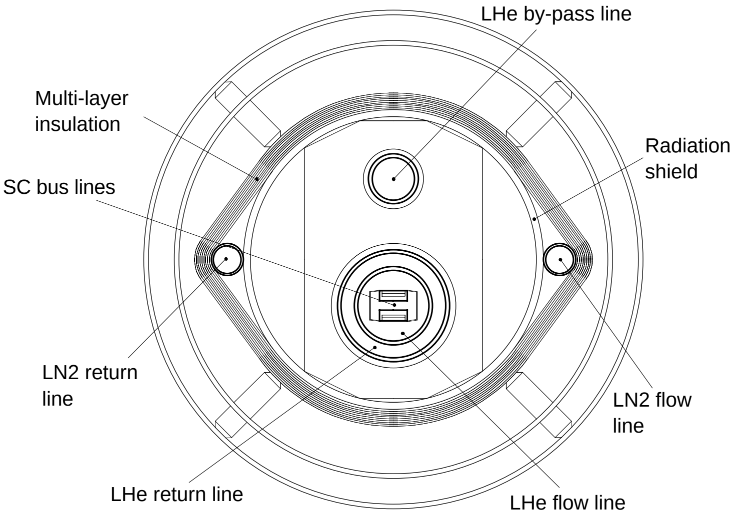

Fig. 11. Cross-section of the multi-channel transfer line.

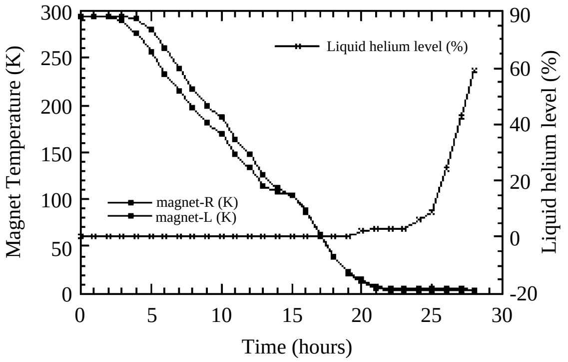

Fig. 12. Cool-down curves of the magnets and liquid-helium level in the sub-cooler.

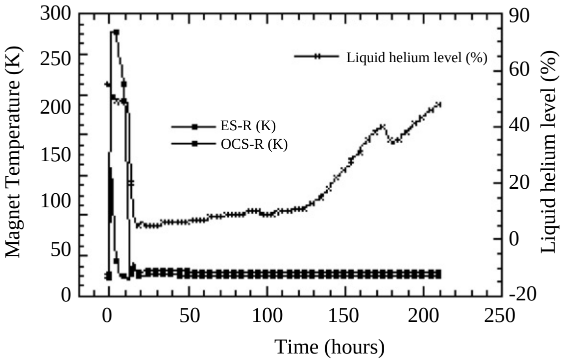

Fig. 13. Recovery from quenches of the S-R and QCS-R magnets.

(40 A, 15 V). Two QCS magnets are excited in series by this power supply, while other magnets have their own power supplies. The quench protection circuit of the QCS magnets is composed of a high-speed SCR switch and two energy dump resistors. The values of the resistors for QCS-R and QCS-L are set at 0.1 and 0.12 Ω, respectively, in order to optimize the time constants of the current decay of these magnets. For quench protection of the other magnets, we selected DC circuit breakers since they did not require rapid decay of the currents in case of quenching. The dump resistors are 0.71 and 2 Ω for the solenoid and correction coil, respectively. The typical quench threshold is set at 1 V for 10 ms or more.

3.8. *Alignment and position monitors*

For the alignment work, four hair-cross targets and a flat base plate are installed on the back of each magnet cryostat. The hair-cross is made of 304 stainless-steel wire of 0.1 mm diameter. Two of the targets are installed on the inner side of the accelerator ring and the other two on the outer side at the same distance from the positron beam

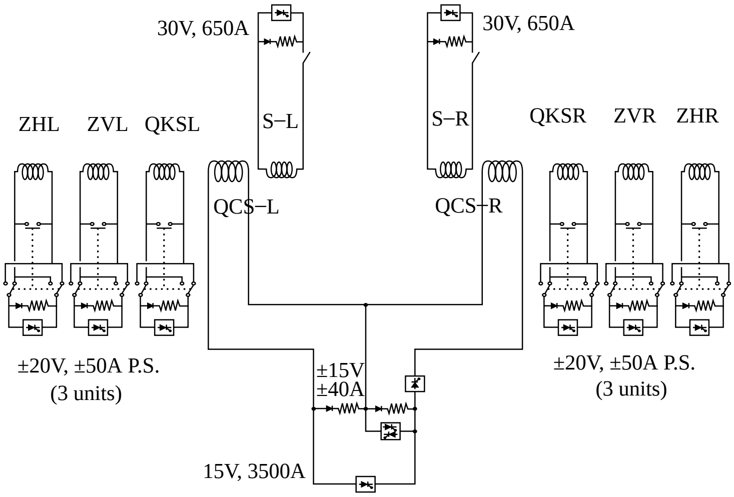

Fig. 14. Electrical circuit of the magnet system.

axis (the center axis of the Belle detector). The separation between the inner and outer targets is 273.34 mm, and the front and rear targets are separated by 400 mm. Their height is 363.13 mm from the beam level. Two pairs of 7 mm-diameter round windows made of 2 mm-thick quartz are installed in the central drift chamber (CDC) end plates, one pair on each side so that the targets on both sides (i.e., four targets in total) can be seen through them. Two QCS magnets (QCS-L and QCS-R) are aligned so that the cross-hair targets on the same inner or outer side of the ring are on the reference line by using a theodolite telescope as well as a leveling telescope. The tilt is adjusted on the flat bases on each QCS magnet. To monitor the movement of the QCS cryostat, four position monitors and a two-directional electric tilt meter are installed on each QCS cryostat. The position monitor measures the capacitance between two electrodes, one of which is installed on the inner surface of the CDC, and the other on the outer surface of the head part of the QCS cryostat. Four position monitors are placed at 90° around the cylindrical part of the QCS cryostat. Signals from these monitors indicate any change in the position, ΔX and ΔY, as well as the rotation of the QCS magnets. A two-directional electric tilt meter is installed on the rear end plate of each QCS cryostat. Signals from the tilt meters indicate any change in the rotation and pitch angles of the QCS magnets.

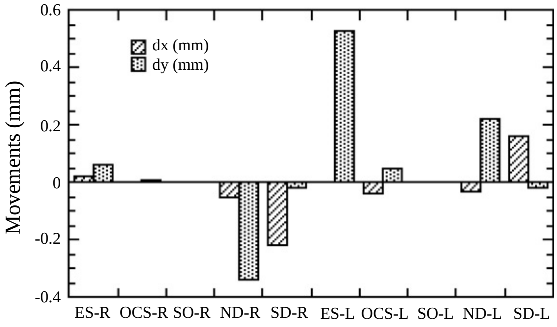

Fig. 15. Movements of the cryostats by excitations of the magnets.

3.9. Operation with the Belle solenoid

Since a large electromagnetic force acts on the magnet cryostat due to interaction with the Belle solenoid field, the cryostat moves slightly, depending on the excitation of the magnets. Fig. 15 shows the transverse movements of the cryostats. In the case of the left-side cryostat, the excitation of S-L up to 487 A induces an upward movement of 0.53 mm. By exciting the normal and skew dipole coils to 50 A, the cryostat moves 0.22 mm vertically and 0.16 mm horizontally. In the case of the right-side cryostat, the movement by S-R

Table 14
Parameters of the KEKB special quadrupole magnets

Item	QC1LE	QC1RE	QC2LE	QC2RE	QC2LP	QC2RP
Field gradient (T/m)	15.60	11.69	3.11	9.99	6.11	2.88
Bore radius (mm)	38	70	60	60	45	42
Pole length (mm)	600	600	2000	600	600	1000
Current density (A/mm^2)	85	12	8	30	17	21
Coil turns (/pole)	3	36	18	10	9	3
Max. current (A)	3000	800	300	1600	800	800
Power (kW)	125	23	11	75	12	8
Flow rate (l/min)	50.0	8.3	7.5	26.7	8.4	7.8
Water lines	12	4	4	4	4	4
Magnet size (mm^W)	600	500	800	900	580	600
(mm^H)	830	800	500	700	410	320
(mm^L)	1100	750	2200	750	720	1080
β_x (m)	20	56	228	341	129	212
β_y (m)	675	1155	304	365	78	69
$x_{\max}$ (mm)	22	29	68	69	57	69
$y_{\max}$ (mm)	21	27	13	16	10	12

$x_{\max}$ and $y_{\max}$ are the maximum amplitudes of the injected beam in the horizontal and vertical planes.

excitation is 0.06 mm. The normal and skew dipole coils move the cryostat by -0.34 mm vertically and -0.22 mm horizontally.

The movement of the cryostat produces a dipole field for the beams. Since the S-R and S-L are operated at constant currents, the dipole fields induced by these excitations are incorporated into Eq. (1). In the case of the correction coils, the operating currents of the normal and skew dipole coils are less than 10 A, so the movements of the cryostats by these coils are much smaller than that of S-L. Therefore, these effects can be neglected in the KEKB operation.

4. Special quadrupole magnets

Six special quadrupole magnets (QC1LE, QC1RE, QC2LE, QC2RE, QC2LP, and QC2RP) are installed in the region where beam separation is very small. Four of these magnets (QC1LE, QC1RE, QC2LE, and QC2RE) are for the HER and two (QC2LP and QC2RP) are for the LER. These magnets were designed to meet the following specifications:

1. The conductor thickness must be minimized; that is, the current density of the coil must be higher than that of an ordinary magnet. In the case of QC1LE, the selected current density was 80 A/mm^2.
2. The magnet must have a field-free channel for the beam of the other ring.
3. A large horizontal aperture with good field quality is required for the large horizontal beta functions in the horizontal focusing quadrupoles.

The required field quality is $\Delta(GL)/GL < \pm 1 \times 10^{-3}$ in the maximum amplitudes of the injected beam for each magnet, which are shown in Table 14.

4.1. Magnet design

Five of the magnets (QC1LE, QC2LE, QC2RE, QC2LP, and QC2RP) were designed as asymmetrical full-quadrupole magnets, whose conductor shape resembles that of a septum magnet. The other magnet (QC1RE) was designed as a half-quadrupole magnet. The parameters of these magnets are listed in Table 14.

Cross-sections of typical special quadrupole magnets are shown in Fig. 16. One beam passes through the quadrupole field center, and the other beam passes the field-free channel in the yoke. In

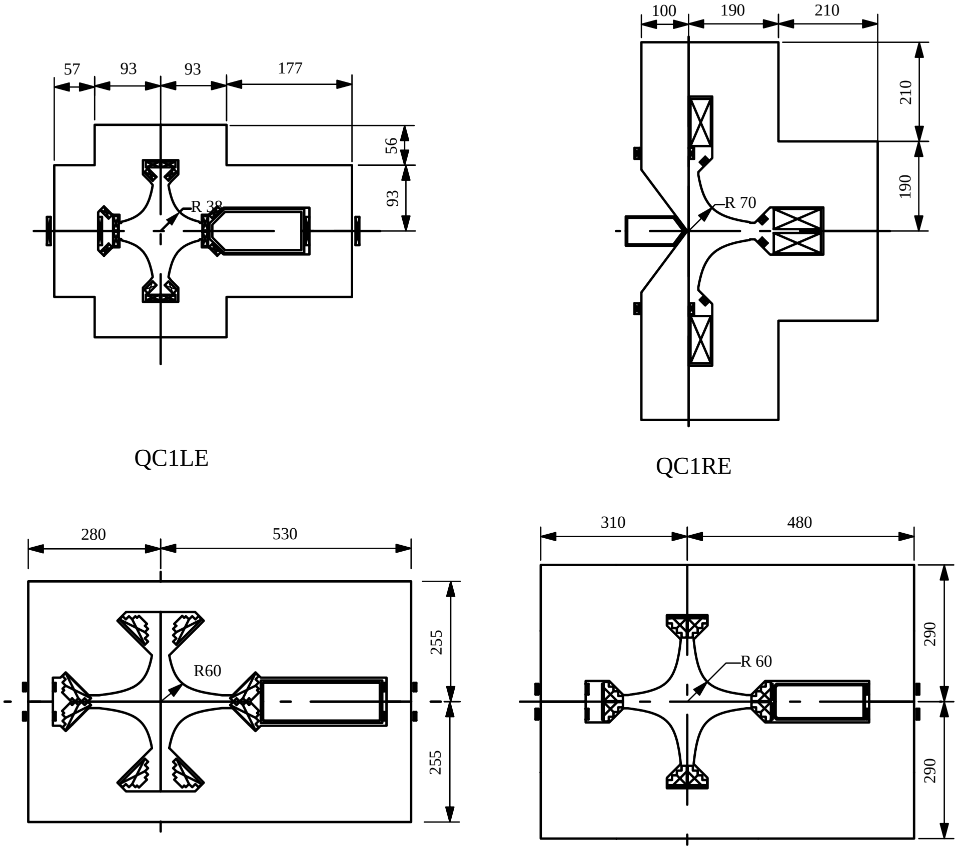

QC1LE

QC1RE

QC2LE

QC2RE

Fig. 16. Cross-sections of some of the special quadrupole magnets for the interaction region.

order to assure a low residual field, a rectangular iron frame was installed in the hole of the yoke. This iron frame works as a magnetic shield, and also as a mechanical support for the coil, on which various forces such as thermal expansion and electromagnetic bursting forces work during excitation.

QC1RE is a half-quadrupole magnet, as is shown in Fig. 16. The iron septum is expected to work as an ideal mirror plate for the magnetic field. The thinnest part of the septum is only 3 mm thick. The design beam orbit in the aperture of QC1RE is separated by about 45 mm horizontally from the surface of the septum. The other beam passes through the field-free region outside the septum.

Because of the lack of quadrupole symmetry of the iron yoke and the truncation of the hyperbolic contour of the poles, the fields of these special quadrupole magnets are likely to have unnecessary multipole components, which may reduce the dynamic aperture. To suppress these multipole components (mainly dipole and sextupole), back-leg coils and trim coils were prepared. The field distributions in these magnets were calculated using the computer code OPERA-2d, and the shape of the pole face shim was optimized.

The horizontal and vertical positions of these magnets, except for QC2LE, can be controlled precisely by the active mover, whose mechanism and movement errors are the same as those of the sextupole magnets in the ring.

4.2. Field measurements and results

The field gradient distribution of these magnets was measured using several harmonic coil systems (coil radius = 10, 35, 55 mm) [12]. The analog signals from these coils were digitized by a dynamic signal analyzer (HP3562A) or Metrolab high-precision integrator (PDI5025). In the case of the QC2 magnets, where the required horizontal aperture was larger than the bore radius, we tried to measure the field distribution by shifting the small harmonic coil ($r = 10$ mm) horizontally. Fig. 17 shows the measurement results of the field distribution of the magnets with end-shim corrections. The ratio of dipole to quadrupole components for QC1RE is 1.06 at $x = 46$ mm. It should be 1 in an ideal case. This may be because the length of the iron septum is not sufficient and the iron septum does not work as an ideal mirror plate at the fringes of the magnet.

The residual field strengths in the field-free space were measured by a Hall probe. They were about 0.5–2 mT for QC1RE and a few tenths of mT for the other magnets. The relatively large leakage field for QC1RE is because of the short iron septum.

4.3. Cooling water system and interlock systems

A special cooling water system for these magnets was developed [13]. A block diagram is shown in Fig. 18. The water temperature is roughly controlled by mixing of hot water returned from the magnets and cold water from a buffer tank, and then finely controlled using heaters. The water temperature can be controlled within ±0.02°C. Since the water-flow speed in the conductor of these magnets is very fast and the temperature of the cooling water is rather high, we paid special care to oxidization of the copper inner surface of the conductor due to the remaining oxygen in the water. To reduce the remaining oxygen, the buffer tank is filled with nitrogen gas and an oxygen removal system using a gas transfer membrane is attached to this system. The dissolved oxygen in water can easily be reduced to less than 30 ppb. As described in the previous section, the coil current density of QC1LE is

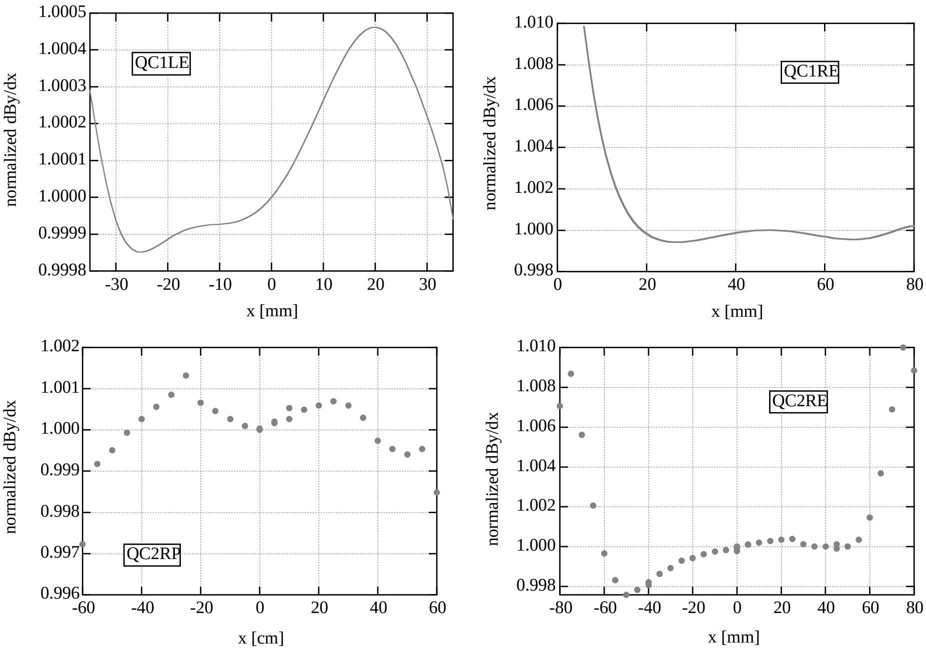

Fig. 17. These graph show the field measurement results of the QC1LE, QC1RE, QC2RP, QC2RE. The field gradient distribution of QC2RP, QC2RE was measured by shifting small radius harmonic coil ($r = 10$ mm) along the horizontal plane.

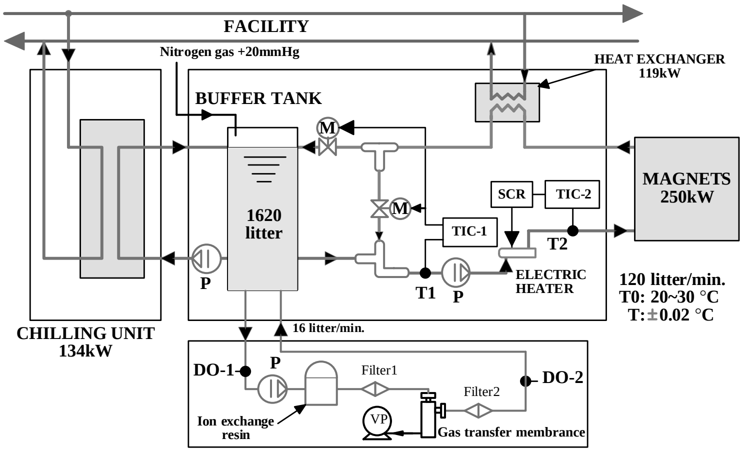

Fig. 18. Block diagram of the cooling water system.

extremely high, 80 A/mm^2. Therefore, it has been protected from burning out by two types of interlock; namely temperature monitors and resistive voltage monitors on each coil.

5. Vacuum chambers

5.1. IP chamber

Precise determination of the decay vertices of *B* mesons using a silicon vertex detector (SVD) is an essential feature of the Belle experiment. Thus, a beam chamber called the IP chamber was constructed together with the SVD [14] for the IP. Fig. 19 shows cross-sectional and top views of the chamber and Fig. 20 shows a close-up view of the central part. The chamber consists of three parts: a central beryllium part, and front and rear aluminum parts. The total length of the IP chamber is 943.5 mm. Since the vertex resolution improves inversely with the distance between the first detection point and the IP, the radius of the chamber should be as small as possible around the IP. The inner radius of the central part of the IP chamber was set at 20 mm by considering the beam background using Monte Carlo simulations. The thickness of the chamber wall near the IP should be as thin as possible in order to reduce the effects of multiple Coulomb scattering in the acceptance of the SVD. The central part ($-50<z<+110$ mm) of the chamber consists of a double-wall beryllium cylinder in order to have helium gas flow in a 2.5 mm gap between the inner and outer cylinders, which is used to cool the beryllium section against heating due to the higher order modes (HOM) rf power. The accelerator vacuum is supported by a 0.5 mm-thick inner cylinder. The outer cylinder is also 0.5 mm thick. The total material thickness of the beryllium cylinders is 0.3% of the radiation length.

HOM rf power analysis predicts about 100 W heat on the inner beryllium cylinder. Assuming that this 100 W heat is uniformly distributed on the inner cylinder, the maximum temperature rise of the inner (outer) beryllium cylinder was estimated to be 25°C (55°C) for a 2 g/s helium flow velocity at 1.5 atm pressure. The measured temperature rise of the outer beryllium cylinder at a total beam current of 1 A was 0.9°C. If the beam charge in a beam bunch is kept constant, the heat can be assumed to be proportional to the total beam current or the total number of beam bunches. Then, the temperature rise of the inner cylinder is expected to be less than 5°C at the KEKB design current (total of 3.6 A), which satisfies the safety condition for the mechanical design of the beam chamber.

These beryllium cylinders are connected to the forward and backward aluminum sections, which

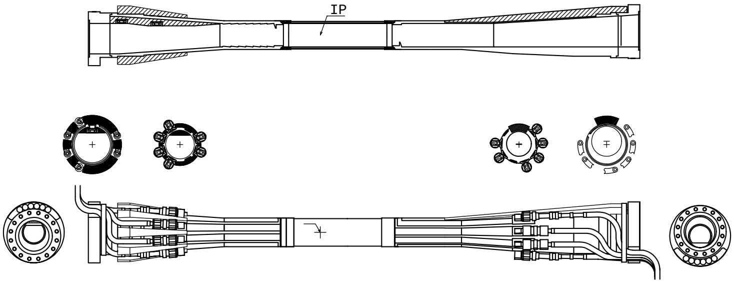

Fig. 19. Cross-sectional and top views of the IP chamber.

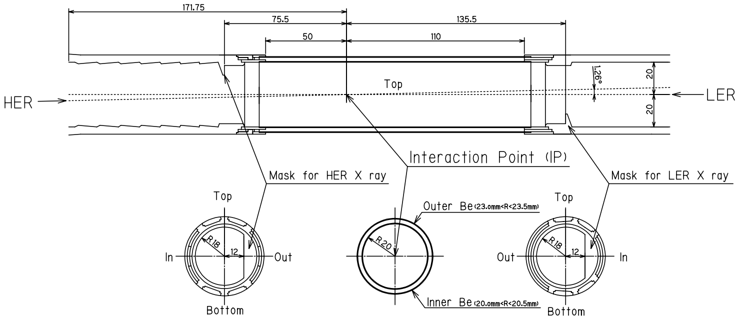

Fig. 20. Central part of the IP chamber.

extend to the IR vacuum chamber. The forward (right side in Fig. 19) and backward (left side in Fig. 19) aluminum sections consist of two parts: one is a cylindrical part, which is welded to the beryllium section through short aluminum rings at both ends; and the other is a conical part, which is connected to the outer vacuum chamber in the QCS cryostat through an aluminum flange. In order to remove about 100 W HOM heating from each of the forward and backward aluminum sections, water channels are embedded in the aluminum parts, and 5 L/min of water is circulated through them.

The SVD is subjected to two types of background from the accelerator: synchrotron radiation (X-rays), and charged particles originally generated by spent electrons and positrons upstream of the IP. Since these backgrounds cause radiation damage to the front-end electronics of the SVD, it should be protected by the IP chamber as much as possible. In order to absorb the synchrotron X-rays which penetrate the IP chamber into the SVD, some thin gold layers were implemented. In the beryllium section, 10 μm-thick gold was sputtered inside the inner beryllium cylinder by evaporating gold in a vacuum before the beryllium cylinder was welded to the aluminum section. This gold thickness amounts to 0.3% of the radiation length. The conical inner shape of the aluminum part allows the synchrotron X-rays generated in the QCS and QC1 magnets to pass through the detector region without hitting the wall of the IP chamber. Two X-ray masks were implemented on the cylindrical part of the aluminum section, as shown in Fig. 20. These are located immediately adjacent to the beryllium section; their maximum height is 8 mm from the inner surface of the cylinder. In addition, as shown in Fig. 20, the inner side of the backward aluminum pipe in the region $-172<z<-76$ mm was machined to have a sawtoothed inner surface in order that any X-rays from the HER upstream might not be scattered into the central part. The height of each sawtooth is 1 mm, and the typical pitch is 13 mm. Gold of 200 μm thickness was chemically plated on the inner surface of the forward aluminum part in order to absorb about 30 keV X-rays, which are generated in the QCS-R magnet, and are backscattered at the inner surface of the vacuum chamber in QC2RE; 20 μm thick gold was also chemically plated on the inner surface of the backward aluminum part in order to absorb about 5 keV X-rays, which are generated upstream of the HER.

In order to absorb the charged-particle backgrounds generated by spent electrons and positrons, three types of particle masks made of tungsten were attached inside and outside of the IP chamber, as shown in Fig. 19. For the particle backgrounds from the HER upstream, two types of tungsten masks are provided inside and outside of the conical part of the backward aluminum section. They are located on the outer side of the accelerator ring only. For the particle backgrounds from the LER, a tungsten mask is provided outside of the conical part of the forward aluminum section. Due to these masks, the SVD can be operated with a total beam current of 1.6 A.

5.2. IR chambers

The vacuum chambers within a ±10 m region from the IP are very different from the standard chambers in the ring. The adoption of a finite crossing angle scheme for the collision makes the final bending magnets unnecessary, thereby avoiding the problem of synchrotron radiation originating from the bend and hitting the crotch part of the vacuum chamber near the IP. On the other hand, the IR quadrupole magnets are not coplanar, and some of the magnets are rotated along the horizontal beam plane. This is because the incoming beam orbit is not parallel to the magnetic field of the detector solenoid. In the design of the vacuum chambers, these points were not taken into account. Thus, the discrepancy had to be absorbed by connecting flanges.

All of the vacuum bellows used for KEKB are equipped with rf bridges inside. In this type, contact fingers are pressed by spring fingers. For the IR, besides this normal type, special short bellows are used to bend the beam duct slightly. Inside this type, a spherical connection is embedded and the flanges are connected with a Helicoflex delta (diameter 3.1/3.2 mm) (Fig. 21).

From the viewpoint of the beam background, the requirements for the vacuum pressure are:

(1) The pressure in the upstream region of the electron beam, 6–50 m from the IP, should be less than 10^{-9} Torr.
(2) The pressure in the upstream region of the positron beam, 4.5 m from the IP and further, should be in the 10^{-10} Torr range.
(3) The pressure at the IP should be less than 10^{-8} Torr.

For the IR vacuum chambers, precise shaping is necessary to provide a sufficient beam aperture. All chambers were made by numerically controlled machine, and were carefully welded to avoid any deformation. In the first design, the chamber body and the flanges were made of aluminum alloy. For the pumps, a non-evaporating getter (NEG) module, a NEG cartridge, and a sputter ion pump were used.

Fig. 22 shows a plan view of the left-side chamber of the IP. The locations of the pumps, gauges, and beam-position monitors (BPMs) are also indicated. Next to the IP chamber is the

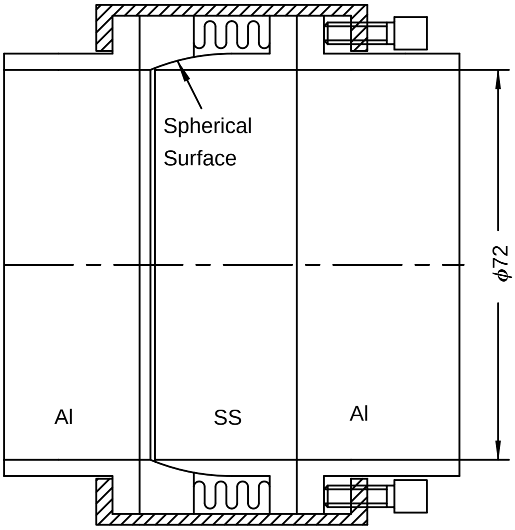

Fig. 21. Schematic drawing of the special short bellows used to bend a beam duct slightly.

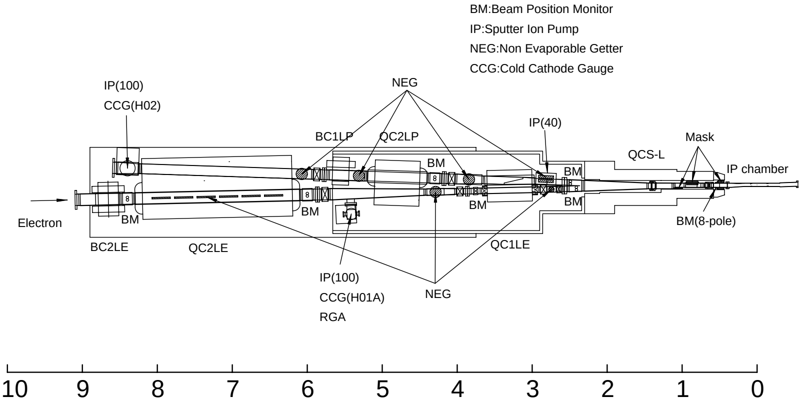

Fig. 22. Plan view of vacuum chambers on the left hand side of IR.

QCS-L chamber, which is placed inside the inner bore of the QCS-L cryostat. The chamber is divided into two parts, with a connection in the middle of the QCS-L cryostat. This is necessary because the front and rear apertures of the chamber are significantly different, and the chamber cannot be passed through the bore of the cryostat when the QCS-L magnet is installed or removed from the Belle detector. In order to connect the two chambers, a special flange has been developed so that they can be remotely connected, as shown in Fig. 23. At the front end (the IP chamber side) of the QCS-L chamber, an 8-electrode BPM module is embedded. In the first design, the feedthroughs were welded to a stainless-steel duct. However, with increasing beam current, heating of the duct due to the wall current was observed. It was, therefore, replaced by a copper duct having an enhanced cooling structure (Fig. 24). In this case, feedthroughs having a stainless-steel outer sheath were directly welded to the copper duct. In the rear half of the QCS-L chamber, two beams are gradually separated (Fig. 25) and a BPM for each beam is installed at the end of the chamber. Since this part of the chamber is made of aluminum, the feedthroughs of the BPMs are attached with flanges.

Synchrotron radiation generated at QCS-L by the outgoing positron beam hits the next vacuum chamber. A large-capacity NEG module is installed in the water-cooled vacuum chamber. Located at QC1LE, this chamber has one duct at the IP side and two ducts at the opposite side. Above this chamber, all chambers are completely separated for the two beams.

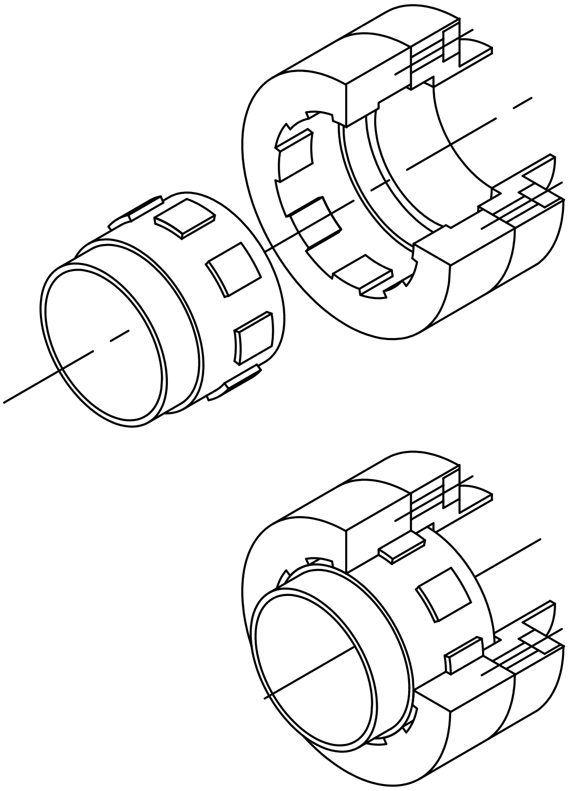

Fig. 23. Conceptual drawing of the special flange to connect two parts of QCS-L chamber in the bore of QCS-L cryostat.

Fig. 26 shows the right side of the IR vacuum chamber. The QCS-R chamber can pass through the inner bore of the QCS-R cryostat. However, the end flange cannot be sufficiently small to pass through the bore. Thus, a demountable flange is used. The front part of the QCS-R chamber is similar to that of the QCS-L chamber. This part is now also made of copper. At the end part of the QCS-R chamber, separation of the two beam ducts is not completed. The two beam ducts are completely separated in the following chamber, and each duct has its own NEG module and BPM.

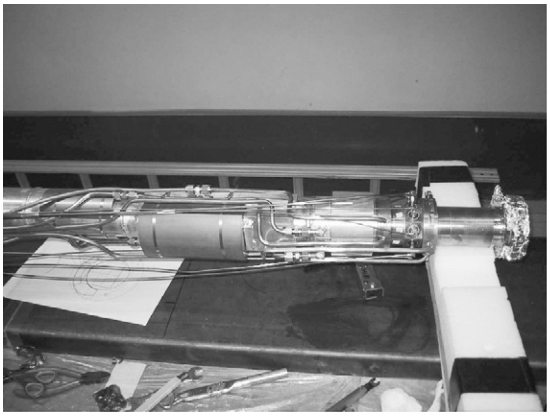

Fig. 24. Front end of the QCS-L chamber.

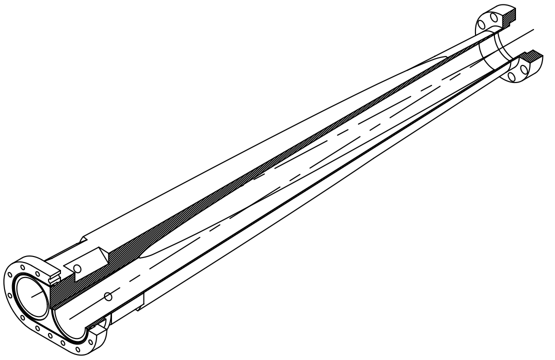

Fig. 25. Original design of the end half of QCS-L chamber.

The QC1RE chamber has a similar structure to that of the QC1LE chamber. The synchrotron radiation from the QCS-R magnet is designed to pass through this chamber, and hits the wall of the next downstream chamber. However, during a collision-tuning operation a temperature rise of this chamber was observed. This is considered to have been caused by synchrotron radiation generated at the IP due to deflection of the electron beams by positron beams. However, why this light hits the chamber is not yet understood. Since the increase in the temperature has a correlation with the luminosity, this chamber is to be remodeled so as to have a good cooling structure. The next long chamber located downstream of the electron beam is the QC2RE chamber. The synchrotron radiation from the QCS-R magnet is expected to pass through its side channel and then hit the wall near its end. The chamber was originally made of aluminum. However, since the backscattered synchrotron radiation is found to be a major background radiation to the detector, it was remade using copper, whose backscattering coefficient is much smaller than that of aluminum.

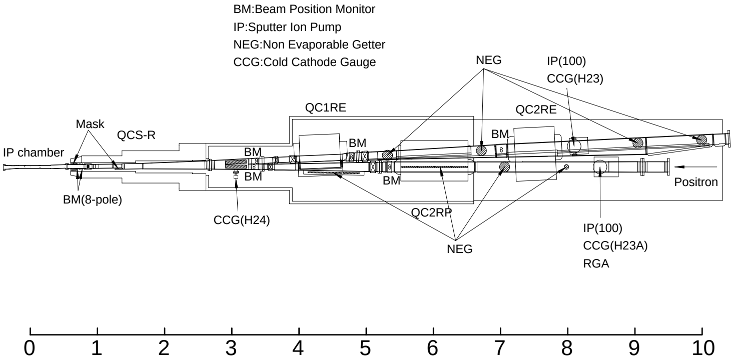

Fig. 26. Plan view of vacuum chambers on the right-hand side of IR.

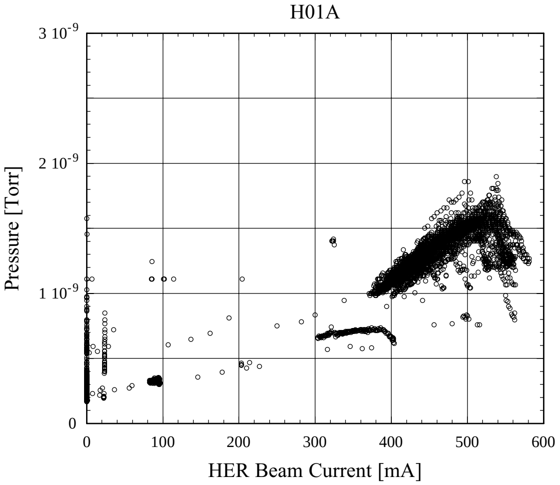

Fig. 27. Pressure variation at CCG(H01A) with respect to the stored current of HER.

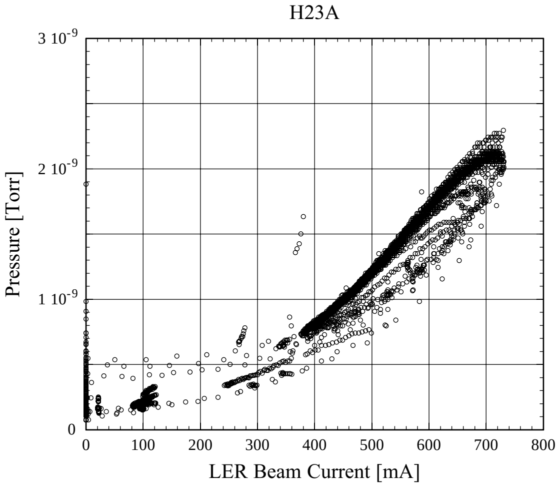

Fig. 28. Pressure variation at CCG(H23A) with respect to the stored current of LER.

The pressure far upstream of the electron beam is well below 10^{-9} Torr. However, the pressure at 5.5 m from the IP changes with the electron-beam current, as shown in Fig. 27. At the present operating current (about 800 mA), the pressure is within the tolerance, but at the design current of KEKB the pressure may go above 10^{-8} Torr. Since the beam background is sensitive to the pressure here, additional pumps will be necessary in the future.

The pressure upstream of the positron beam (8.5 m from the IP) does not satisfy the requirement (Fig. 28). At present, the beam background due to the positron beam is at a tolerable level, though some measures to lower the pressure will be necessary in the near future.

Another problem is heating of the vacuum chamber. Some parts, such as the QC1RE chamber, are unexpectedly heated up, and some parts are heated up by synchrotron radiation from (weak) bends outside the IR, which was neglected in the first design. With increasing beam current this will become a serious problem. The most urgent problem is a temperature rise of the side mask of both QCS chambers, which are located inside the bores of the QCS cryostats. A cooling structure will be added when a major revision of the IR chamber is made. Also, the heating of some bellows has been observed. A typical case is seen at the bellows of the positron duct of the QC1RE chamber. This will be cooled at the same time as remodeling of the electron duct is carried out. Another delicate problem is the movement of the chambers, especially that of the QCS chambers. Since these chambers are not fixed tightly, the heating of various parts of the chambers causes a movement on the order of 100 μm. This is a crucial problem because the BPMs of these chambers are used to control the beam position at the IP. At present, the movement is measured by a position sensor, and the readings of the BPMs corrected with the signals are used to control the collision condition.

6. Summary

The interaction region of the KEK B-Factory, which has a finite crossing angle, has been operated during the past 3 years. All components of this region have been working fairly stably, and it was confirmed that the design and construction of the IR was well performed in spite of its challenging trials; i.e., the superconducting final focusing system, a special quadrupole magnet with an extremely high-current density coil, and a special joint-structure of the vacuum chamber. In particular, the superconducting magnet system has been working very reliably without any serious problems. Its total operating time has reached about 1900 h. However, some problems begin to appear in the vacuum system as the beam current increases, namely heating and movement of the vacuum chamber. In order to achieve a much higher beam current, some parts of the vacuum chambers should be improved so that they can tolerate a much higher heat flux by synchrotron radiation.

Acknowledgements

The authors would like to express their gratitude to Prof. Shin-ichi Kurokawa for his continuous support and encouragement in this work. We also thank our colleagues at KEK for their enthusiastic contributions to the design, construction and operation. They are also very grateful to Dr. E. Kikutani for performing the editorial task. Finally, our thanks go to the employees of Hitachi Ltd., Ishikawajima–Harima Heavy Industries Co., Ltd., and Mitsubishi Electric Corp. for their responsible and skilful work.

References

[1] KEKB B-Factory Design Report, KEK Report 95-7, 1995.

[2] Y. Funakoshi, et al., Proceedings of the Seventh European Particle Accelerator Conference (EPAC2000), 2000, p. 28.

[3] Y. Makida, et al., IEEE Trans. Appl. Supercond. 9 (2) (1999) 475.

[4] K. Tsuchiya, et al., Proceedings of the Fifth European Particle Accelerator Conference (EPAC96), 1996, p. 2287.

[5] K. Tsuchiya, et al., IEEE Trans. Appl. Supercond. 9 (2) (1999) 1045.

[6] K. Tsuchiya, et al., presented at Particle Accelerator Conference (PAC2001), Chicago, June 18–22, 2001.

[7] A. Morgillo, et al., Proceedings of the 1995 PAC and International Conference on High-Energy Accelerators, p. 1393.

[8] N. Ohuchi, et al., Proceedings of the e^+e^- Factories 99, KEK Proc. 99-24, 2000, p. 217.

[9] N. Ohuchi, et al., Proceedings of the Sixth European Particle Accelerator Conference (EPAC98), 1998, p. 2002.

[10] N. Ohuchi, et al., Adv. Cryogenic Eng. 45A (2000) 787.

[11] K. Tsuchiya, et al., Adv. Cryogenic Eng. 37 (Part A) (1992) p. 667.

[12] M. Tawada, H. Nakayama, K. Satoh, Proceedings of the Seventh European Particle Accelerator Conference, EPAC2000, 2000, p. 2128.

[13] M. Yoshioka, et al., Proceedings of the First Asian Particle Accelerator Conference, APAC98, Vol. 260, 1998.

[14] Belle SVD group, Nucl. Instr. and Meth. A 453 (2000) 71.